





Cite this: *RSC Adv.*, 2021, **11**, 7587

# Highly crystalline anatase TiO<sub>2</sub> nanocuboids as an efficient photocatalyst for hydrogen generation†

Shubhangi R. Damkale,  Sudhir S. Arbuj,  Govind G. Umarji, Sunit B. Rane and Bharat B. Kale \*

Highly crystalline anatase titanium dioxide (TiO<sub>2</sub>) nanocuboids were synthesized *via* a hydrothermal method using ethylenediamine tetraacetic acid as a capping agent. The structural study revealed the nanocrystalline nature of anatase TiO<sub>2</sub> nanocuboids. Morphological study indicates the formation of cuboid shaped particles with thickness of ~5 nm and size in the range of 10–40 nm. The UV-visible absorbance spectra of TiO<sub>2</sub> nanocuboids showed a broad absorption with a tail in the visible-light region which is attributed to the incorporation of nitrogen atoms into the interstitial positions of the TiO<sub>2</sub> lattice as well as the formation of carbonaceous and carbonate species on the surface of TiO<sub>2</sub> nanocuboids. The specific surface areas of prepared TiO<sub>2</sub> nanocuboids were found to be in the range of 85.7–122.9 m<sup>2</sup> g<sup>−1</sup>. The formation mechanism of the TiO<sub>2</sub> nanocuboids has also been investigated. Furthermore, the photocatalytic activities of the as-prepared TiO<sub>2</sub> nanocuboids were evaluated for H<sub>2</sub> generation *via* water splitting under UV-vis light irradiation and compared with the commercial anatase TiO<sub>2</sub>. TiO<sub>2</sub> nanocuboids obtained at 200 °C after 48 h exhibited higher photocatalytic activity (3866.44 μmol h<sup>−1</sup> g<sup>−1</sup>) than that of commercial anatase TiO<sub>2</sub> (831.30 μmol h<sup>−1</sup> g<sup>−1</sup>). The enhanced photoactivity of TiO<sub>2</sub> nanocuboids may be due to the high specific surface area, good crystallinity, extended light absorption in the visible region and efficient charge separation.

Received 22nd December 2020  
Accepted 5th February 2021

DOI: 10.1039/d0ra10750f

rsc.li/rsc-advances

## 1. Introduction

Titanium dioxide (TiO<sub>2</sub>) has attracted tremendous attention in the last few decades due to its potential applications in the field of photocatalysis for solar fuel production and environmental remediation.<sup>1,2</sup> Photocatalytic hydrogen production over semiconductors is an effective and attractive method for the conversion of solar energy to clean and renewable hydrogen fuel.<sup>3–6</sup> Since the first report by Fujishima and Honda in 1972 on the photo-assisted decomposition of water into hydrogen and oxygen using a TiO<sub>2</sub> photoanode in the electrochemical cell,<sup>7,8</sup> extensive research has been carried out to investigate various semiconductor oxides as well as sulphides as photocatalysts for energy and environment related applications.<sup>9,10</sup> Among the reported semiconductor photocatalysts, *viz.* ZnO, TiO<sub>2</sub>, SnO<sub>2</sub>, Nb<sub>2</sub>O<sub>5</sub>, CdS and ZnS, TiO<sub>2</sub> is more superior and a benchmark photocatalyst owing to its chemical inertness, appropriate band edge positions, high photostability, low cost and nontoxicity.<sup>1,10–13</sup>

TiO<sub>2</sub> mainly exists in the three different crystalline forms; anatase, rutile and brookite. During the past years, many

investigations have confirmed anatase TiO<sub>2</sub> is generally photocatalytically more active than rutile TiO<sub>2</sub> because its larger band gap (3.2 eV) compared to that of rutile (3.0 eV) corresponds to a stronger redox ability.<sup>14</sup> In the crystal structure of anatase, the primary TiO<sub>6</sub> octahedron building units are significantly distorted and interconnected *via* corner and edge sharing to form zigzag chains with a screw axis. Compared with the other two phases, such a structure offers a relatively loose atomic stacking and less density that may be correlated with its greater absorption capability and more abundant active sites (oxygen vacancies).<sup>15</sup> However, the wide band gap of the anatase TiO<sub>2</sub> and the high recombination rate of photogenerated charge carriers have severely restricted the efficiency of TiO<sub>2</sub>.<sup>16</sup> Currently, several strategies such as metallic or nonmetallic ion doping<sup>13,16–19</sup> noble metal deposition<sup>20–22</sup> and coupling with other semiconductors<sup>23–25</sup> are developed to extend its photo-response to visible light or to improve the charge separation. Besides these methods, morphological modification is another adopted method.<sup>26,27</sup> Du *et al.* reported that photocatalytic performance also depends on the exposed facets of TiO<sub>2</sub>.<sup>28,29</sup>

The photoactivity of TiO<sub>2</sub> is found to be greatly influenced by a variety of factors including crystalline phase, specific surface area, crystallinity, photon absorption properties and so on.<sup>1,30</sup> Anatase TiO<sub>2</sub> with higher crystallinity is preferred for photocatalysis, since higher crystallinity would mean fewer defects for the recombination of photogenerated electrons and holes.<sup>31</sup>

Centre for Materials for Electronics Technology (C-MET), Off Pashan Road, Panchawati, Pune-411008, Maharashtra, India. E-mail: bbkale1@gmail.com; bbkale@cmet.gov.in; Fax: +912025898180; Tel: +912025899273

† Electronic supplementary information (ESI) available. See DOI: 10.1039/d0ra10750f



Generally, semiconductor based photocatalysis proceeds through following three steps: (1) absorption of light; (2) separation and transport of charge carriers; and (3) redox reactions on the surface of the semiconductor.<sup>32</sup> Since the photocatalytic reactions mainly take place on the surface of photocatalysts, the large surface area is generally favorable to enhance the photocatalytic activity during photocatalysis. Therefore it is crucial to control the particle size as well as morphology of the photocatalyst in order to increase its applicability.<sup>1,33,34</sup> Over the past decades, a variety of controlled synthesis methods such as sol-gel,<sup>35,36</sup> hydrothermal,<sup>37,38</sup> microwave-assisted<sup>39</sup> and chemical vapour deposition<sup>40</sup> have been attempted to synthesize TiO<sub>2</sub> nanostructures with varied morphologies. When compared to the other methods, the hydrothermal method not only enables obtaining materials with a large surface area and high crystallinity but also flexibly adjust the parameters to control the particle size and morphology of products.<sup>41</sup>

So far, numerous morphologies of TiO<sub>2</sub> nanostructures *viz.*, nanowires,<sup>42</sup> nanotubes,<sup>43</sup> nanobelts,<sup>44</sup> nanorods,<sup>45,46</sup> nanosheets,<sup>47</sup> nanoflowers,<sup>48,49</sup> hierarchical microspheres<sup>50</sup> have been effectively synthesized by hydrothermal technique. Moreover, many researchers have exploited the synthesized TiO<sub>2</sub> nanostructures for the photocatalytic hydrogen generation. For example, Yu *et al.*<sup>51</sup> have synthesized anatase TiO<sub>2</sub> nanosheets by a simple hydrothermal treatment of the mixed solution of tetrabutyl titanate and hydrofluoric acid which exhibited much higher photocatalytic H<sub>2</sub> production activity than Degussa P25 TiO<sub>2</sub>. Flower-like anatase TiO<sub>2</sub> nanosheets fabricated by Jitputti *et al.*<sup>52</sup> using hydrothermal process on amorphous TiO<sub>2</sub> spheres obtained by controlled hydrolysis of titanium isopropoxide in ethanol also showed high photocatalytic activity for H<sub>2</sub> evolution than that of commercial anatase TiO<sub>2</sub> powder after heat treatment. Furthermore, Cheng and co-workers<sup>53</sup> also reported that twinned anatase TiO<sub>2</sub> nanocrystals synthesized by a facile hydrothermal method from hydrolysis of titanium glycolate powder precursor exhibited significantly larger photocatalytic activity towards H<sub>2</sub> production than that of commercial TiO<sub>2</sub> (P25 Degussa). However, many studies have been focused on improving the photocatalytic activity by fabricating TiO<sub>2</sub> with large specific surface area, high crystallinity, enhanced light absorption and so on.

In this regard, herein, we demonstrate a facile synthesis method to prepare highly crystalline 3D TiO<sub>2</sub> nanocuboids having high specific surface area. A titanium precursor was prepared from commercial anatase TiO<sub>2</sub> powder and employed to synthesize TiO<sub>2</sub> nanocuboids *via* a one-pot hydrothermal reaction using EDTA as the capping agent. The hydrothermal reactions were carried out at different time and temperature conditions. The photocatalytic activities of the as prepared TiO<sub>2</sub> nanocuboids were investigated for H<sub>2</sub> generation *via* water splitting and also compared with the commercial anatase TiO<sub>2</sub>.

## 2. Experimental section

### 2.1. Materials

Commercial titanium dioxide (TiO<sub>2</sub>) powder (99.8%, anatase) was purchased from Sigma-Aldrich. Hydrofluoric acid (HF,

40 wt%) was obtained from S. D. Fine Chemicals Ltd, hydrogen peroxide (H<sub>2</sub>O<sub>2</sub>, 30 wt%), ammonia (NH<sub>3</sub>, about 25%) and ethylenediamine tetraacetic acid (EDTA) were all purchased from Fisher Scientific. All the chemicals were used as received without further purification.

### 2.2. Synthesis of titanium dioxide nanocuboids (TiO<sub>2</sub> NCs)

Commercial TiO<sub>2</sub> powder was employed as the starting material. In a typical synthesis, firstly, 25.0 mmol of TiO<sub>2</sub> powder was dissolved in 25 mL of hydrofluoric acid by heating the mixture in Teflon lined autoclave at 150 °C for 3 h. After cooling the autoclave at room temperature, the reaction mass was again re-precipitated by adding 50 mL of ammonia. The obtained white precipitate was then washed thoroughly with deionized (DI) water to remove excess NH<sub>4</sub><sup>+</sup> and F<sup>−</sup> ions. Furthermore, this precipitate was again dissolved in a 60 mL solution containing 50 mL hydrogen peroxide and 10 mL ammonia (5 : 1 by volume) under continuous stirring to get a precursor. To the precursor solution, 12.5 mmol of ethylenediamine tetraacetic acid (EDTA) was added and this mixture was heated at 60 °C for 1 h to promote the decomposition of H<sub>2</sub>O<sub>2</sub> and then was transferred into a Teflon-lined stainless steel autoclave. The autoclave was sealed, heated at 200 °C for 24 h and then cooled to room temperature naturally. The resultant precipitate was collected by centrifugation, washed several times with DI water followed by ethanol and dried in an oven at 60 °C overnight. The same procedure was followed to prepare TiO<sub>2</sub> nanocuboids at different reaction time and temperature conditions *i.e.* 48 h, 150 °C; 48 h, 180 °C and 48 h, 200 °C. The obtained TiO<sub>2</sub> nanocuboids were named as TiO<sub>2</sub>-NCs 24 h, 200 °C; TiO<sub>2</sub>-NCs 48 h, 150 °C; TiO<sub>2</sub>-NCs 48 h, 180 °C and TiO<sub>2</sub>-NCs 48 h, 200 °C.

### 2.3. Characterization

X-ray powder diffraction (XRD) patterns were obtained by using a Bruker D8 Advance X-ray powder diffractometer with Cu-K $\alpha$  radiation in the 2 $\theta$  range of 20°–80°. The surface morphology of the samples was characterized by field-emission scanning electron microscopy (FESEM, HITACHI S-4800). TEM micrographs were recorded on a field-emission transmission electron microscopy (FETEM, JEOL JEM-2200FS) at an operating voltage of 200 kV. High-resolution TEM (HRTEM) and selected area electron diffraction (SAED) were also recorded on JEOL JEM-2200FS. X-ray photoelectron spectroscopy (XPS) measurement was performed on a Thermo Scientific ESCALAB 250Xi X-ray spectrometer using an Al K $\alpha$  radiation at 1486.6 eV. Fourier transform infrared (FTIR) spectroscopy measurements were carried out with a Jasco FTIR-6100 spectrometer over a range of 400–4000 cm<sup>−1</sup>. UV-vis diffuse reflectance spectra were recorded at room temperature in the range 200–800 nm using Shimadzu UV-Vis-NIR spectrophotometer (Model UV-3600). The Brunauer–Emmett–Teller (BET) specific surface areas of the samples were calculated from the N<sub>2</sub> adsorption isotherms at liquid N<sub>2</sub> temperature using Quantachrome NOVA touch LX<sup>1</sup> instrument. The samples were degassed in vacuum at 150 °C for 2 h prior to BET analysis. Photoluminescence (PL) spectra were detected with a Shimadzu RF-5301pc spectrofluorophotometer.



The photoconductivity experiments were carried out under solar simulator (Photo Emission Technology, Model: #SS50AAA) integrated with Keithley 4200SCS system.

#### 2.4. Photocatalytic hydrogen generation test

The photocatalytic hydrogen evolution experiments were carried out in a closed reactor system under UV-vis light irradiation using 400 W mercury vapor lamp. The reactor used in the photocatalytic process was a 100 mL cylindrical quartz vessel. The system was well sealed with septum arrangement to remove the evolved gas through gas-tight syringe for quantifying the amount of gases evolved. In a typical photocatalytic experiment, 20 mg of  $\text{TiO}_2$  catalyst powder having 1 wt% preloaded platinum as a co-catalyst was suspended in 30 mL solution containing 25 mL deionized water and 5 mL methanol. Before irradiation, the nitrogen gas was bubbled through the reaction mixture in order to remove the dissolved gases. Magnetic stirring of the solution was maintained throughout the experiment in order to keep the photocatalyst particles in suspension status. A 0.5 mL of evolved gas was sampled intermittently through the septum, and hydrogen was analyzed using a gas chromatograph (Shimadzu: Model GC 2014) equipped with 5 Å molecular sieves column. The amount of hydrogen produced was calculated according to the fitted standard curve. Cyclic stability of the most active sample was tested by repeating the photocatalytic reaction three times under identical conditions.

### 3. Results and discussion

#### 3.1. Structural analysis

Fig. 1 shows the X-ray diffraction patterns of commercial  $\text{TiO}_2$  and  $\text{TiO}_2$  NCs prepared under different reaction time and temperature conditions. As shown in figure, XRD pattern of commercial  $\text{TiO}_2$  shows characteristic diffraction peaks located at  $2\theta = 25.3^\circ, 37.8^\circ, 48.0^\circ, 53.9^\circ, 55.0^\circ, 62.7^\circ, 68.7^\circ, 70.3^\circ$ , and  $75.0^\circ$  corresponding to the (101), (004), (200), (105), (211), (204), (116), (220) and (215) planes of tetragonal anatase  $\text{TiO}_2$  (JCPDS card no. 21-1272), respectively.  $\text{TiO}_2$  NCs prepared at different reaction conditions also show similar diffraction patterns with a slight change in the peak position of the (101) plane.

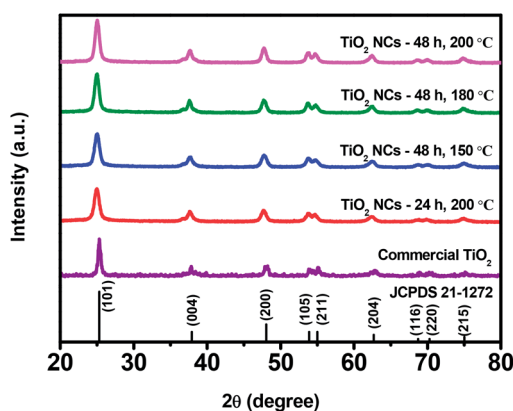


Fig. 1 XRD patterns of commercial  $\text{TiO}_2$  and  $\text{TiO}_2$  nanocuboids prepared under different reaction time and temperature conditions.

The relatively broad XRD peaks of the as prepared  $\text{TiO}_2$  NCs as compared to the commercial  $\text{TiO}_2$  sample reveals that the  $\text{TiO}_2$  NCs obtained at different reaction conditions have a smaller size. It can be seen that the intensity of the (101) diffraction peak of as prepared  $\text{TiO}_2$  NCs increases slightly with increasing hydrothermal reaction time and temperature.

Fig. 2 illustrates magnified (101) peak of commercial  $\text{TiO}_2$  and as prepared  $\text{TiO}_2$  NCs. As can be seen, a slight shift in the peak position of the (101) plane to lower  $2\theta$  value is noticed with all of the as prepared  $\text{TiO}_2$  NCs compared to commercial  $\text{TiO}_2$  sample. The shift in the  $2\theta$  value infers that stress has occurred due to doping of other atoms into the lattice of as prepared  $\text{TiO}_2$  NCs and it is discussed in the XPS analysis section.<sup>54</sup>

The average crystallite sizes of the commercial  $\text{TiO}_2$  and as prepared  $\text{TiO}_2$  NCs were estimated by the Scherrer's formula. The average crystallite size of commercial  $\text{TiO}_2$  was found to be 17.3 nm, whereas for  $\text{TiO}_2$  NCs prepared under different time and temperature conditions *i.e.* 24 h, 200 °C; 48 h, 150 °C; 48 h, 180 °C and 48 h, 200 °C, the average crystallite sizes were found to be 10.2, 10.3, 11.2 and 11.6 nm, respectively. The relative crystallinity of the as prepared  $\text{TiO}_2$  NCs was also quantitatively evaluated *via* the relative intensity of (101) diffraction peak of  $\text{TiO}_2$  NCs prepared at 200 °C for 24 h. The relative crystallinity of the  $\text{TiO}_2$  samples is listed in Table 1. It was observed that the average crystallite size and relative crystallinity of as prepared  $\text{TiO}_2$  NCs increases with increasing reaction time and temperature.

#### 3.2. Morphological analysis

Fig. 3 displays the FESEM images of commercial  $\text{TiO}_2$  and as prepared  $\text{TiO}_2$  NCs. The commercial  $\text{TiO}_2$  powder exhibits irregularly-shaped particles with a size in the range of 50–200 nm (Fig. 3a). However, after hydrothermal treatment under different time and temperature conditions and with EDTA capping, commercial  $\text{TiO}_2$  shows a significant morphological transition from irregular large particles to very small sized particles. Since the particle size of as prepared  $\text{TiO}_2$  nanostructures is too small, its morphology and size cannot be

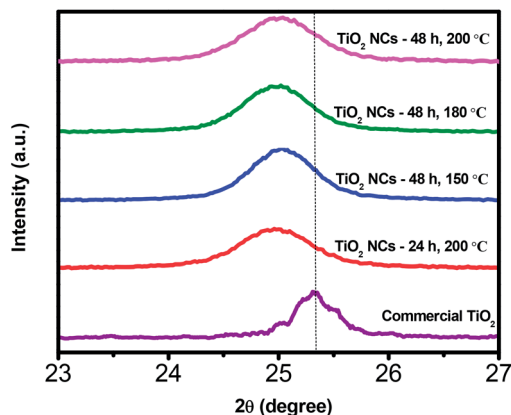


Fig. 2 Magnified XRD patterns of (101) plane of commercial  $\text{TiO}_2$  and  $\text{TiO}_2$  nanocuboids prepared under different reaction time and temperature conditions.



**Table 1** Relative crystallinity, band gap, specific surface area and H<sub>2</sub> generation in  $\mu\text{mol h}^{-1} \text{g}^{-1}$  of commercial TiO<sub>2</sub> and as prepared TiO<sub>2</sub> nanocuboids

Sample	Relative crystallinity <sup>a</sup>	Band gap (eV)	Specific surface area ( $\text{m}^2 \text{g}^{-1}$ )	H <sub>2</sub> generation ( $\mu\text{mol h}^{-1} \text{g}^{-1}$ )
Commercial TiO <sub>2</sub>	—	3.27	29.3	831.30
TiO <sub>2</sub> -NCs 24 h, 200 °C	1	3.24	122.9	1706.40
TiO <sub>2</sub> -NCs 48 h, 150 °C	1.02	3.20	111.6	1924.31
TiO <sub>2</sub> -NCs 48 h, 180 °C	1.17	3.16	103.2	2954.78
TiO <sub>2</sub> -NCs 48 h, 200 °C	1.28	3.12	85.7	3866.44

<sup>a</sup> Relative crystallinity is calculated using the ratio of intensity of diffraction peak from the (101) plane of anatase TiO<sub>2</sub> NCs prepared under different reaction conditions to the intensity of the (101) peak of TiO<sub>2</sub> NCs prepared for 24 h at 200 °C.

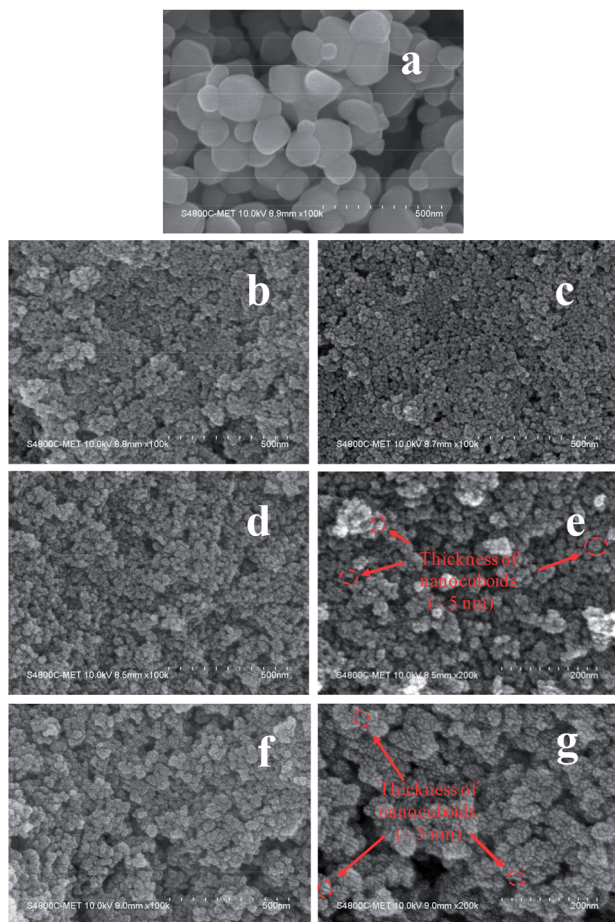


**Fig. 3** FE-SEM images of (a) commercial TiO<sub>2</sub> and TiO<sub>2</sub> nanocuboids prepared under different reaction time and temperature conditions: (b) 24 h, 200 °C; (c) 48 h, 150 °C; (d and e) 48 h, 180 °C and (f and g) 48 h, 200 °C.

clearly determined from Fig. 3b–d and f. However, slightly high-magnification FESEM images (Fig. 3e and g) distinctly shows that the TiO<sub>2</sub> nanostructures are composed of cuboid-like particles having a thickness of ~5 nm (as marked in the Fig. 3e and g) and size in the range of 10–20 nm. Further, the FETEM was used to confirm the morphology and size of nanoparticles as well as to examine the crystal structure of the TiO<sub>2</sub> nanoparticles.

Fig. 4 shows the FETEM images, high resolution TEM (HRTEM) images and the corresponding selected area electron diffraction (SAED) patterns of the commercial TiO<sub>2</sub> and as prepared TiO<sub>2</sub> NCs. FETEM image (Fig. 4a) confirms the irregular shaped morphology of commercial TiO<sub>2</sub>. The size of the particles is in the range of 50 to 200 nm as observed by FESEM analysis. The HRTEM image indicate an equal lattice spacing of 0.35 nm corresponding to the (101) and (−101) planes of anatase TiO<sub>2</sub>. The selected area electron diffraction (SAED) pattern (Fig. 4c) shows single crystalline nature of commercial TiO<sub>2</sub> along with (101) and (−101) planes.

Fig. 4d and g shows the FETEM images of TiO<sub>2</sub> NCs prepared for 48 h at 150 and 200 °C respectively. FETEM images clearly show that the as prepared TiO<sub>2</sub> nanostructures are composed of cuboid shaped particles. However, as seen from Fig. 4d and g, the increase of the reaction temperature from 150 to 200 °C, leads to increase in the particle size range from 10–20 nm to 10–40 nm. Fig. 4e and h shows the HRTEM images of TiO<sub>2</sub> NCs

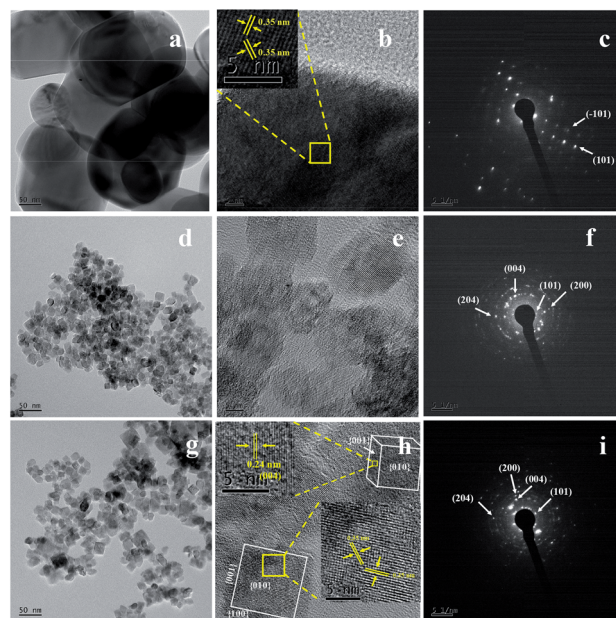


**Fig. 4** FE-TEM images, HRTEM images and corresponding SAED patterns of commercial TiO<sub>2</sub> and as prepared TiO<sub>2</sub> nanocuboids: (a–c) commercial TiO<sub>2</sub>, (d–f) TiO<sub>2</sub> nanocuboids prepared for 48 h at 150 °C; (g–i) TiO<sub>2</sub> nanocuboids prepared for 48 h at 200 °C.



prepared for 48 h at 150 and 200 °C respectively. As shown in the inset of Fig. 4h, a magnified view of the selected region of single cuboid  $\text{TiO}_2$  nanocrystal displays visible lattice fringes with  $d$  spacings of 0.35 nm, which can be indexed to (101) plane of anatase  $\text{TiO}_2$ . A similar  $d$  spacing of 0.35 nm observed at an angle of  $136.6^\circ$  to (101) plane can be indexed to  $(-101)$  plane.<sup>55</sup> According to the crystallographic knowledge and imaging theory of TEM, the exposed facet (010) of  $\text{TiO}_2$  is perpendicular to these two crystal facets so that  $\text{TiO}_2$  nanocrystal is faced with {010} crystal facet, with {001} and {100} facets forming the lateral sides. Also as shown in the inset of Fig. 4h, the edge to the {010} facet is marked with  $d$  spacing of 0.24 nm that can be indexed to (004) planes of exposed {001} facet. This indicates that anatase  $\text{TiO}_2$  nanocrystals are exposed with high energy {010}, {100} and {001} facets.<sup>56,57</sup>

The corresponding SAED patterns of the as prepared  $\text{TiO}_2$  NCs exhibit a polycrystalline nature. The distinct diffraction rings of the SAED patterns confirm the presence of well-crystallized anatase as shown in Fig. 4f and i. The diffraction ring spots can be indexed as (101), (004), (200) and (204) crystal planes of anatase  $\text{TiO}_2$  which is in accordance with the XRD results (Fig. 1).

### 3.3. XPS analysis

The X-ray photoelectron spectroscopy (XPS) analysis was performed to study the surface chemical composition of  $\text{TiO}_2$  NCs prepared at 200 °C for 48 h and the results are presented in Fig. 5. The wide scan survey spectrum (Fig. 5a) showed that the  $\text{TiO}_2$  NCs contain C, N, Ti, O and F elements, with photoelectron peaks appearing at binding energies of 285.82 (C 1s), 400.09 (N 1s), 458.92 (Ti 2p), 530.15 (O 1s) and 683.88 eV (F 1s) respectively.

The high-resolution C 1s spectrum (Fig. 5b) indicated one broad peak, which can be well fitted to three peaks, located at 284.58, 285.95 and 287.90 eV. The strongest peak at the binding energy of 284.58 eV corresponds to graphitic or  $\text{sp}^2$  carbon atoms ( $\text{sp}^2 \text{C}=\text{C}$ )<sup>58,59</sup> and is thought to signal the presence of elemental carbon including the coke-like carbonaceous species at the surface of titania nanoparticles as well as adventitious carbon.<sup>60,61</sup> Whereas the peak at 285.95 eV can be assigned to  $\text{sp}^2$  carbon–nitrogen bondings ( $\text{N}-\text{sp}^2 \text{C}$ ).<sup>58,62</sup> The nitrogen atoms in the C–N bonds might be from the precursor or from capping agent EDTA. Further, the small peak at 287.90 eV is attributed to  $\text{C}=\text{O}$  bond.<sup>63,64</sup> Several studies have attributed the C dopants to carbonate species present on the  $\text{TiO}_2$  surface in the form of  $\text{Ti}-\text{O}=\text{C}$  linkages.<sup>65</sup> However, the absence of a peak around 281–282 eV intrinsically resulting from a Ti–C bonding ( $\text{O}-\text{Ti}-\text{C}$  linkage) indicates that carbon does not substitute the oxygen atoms in the lattice of  $\text{TiO}_2$  (substitutional C-doping).<sup>66</sup> Also, no peak at around 288.6 eV suggests that there is no possibility of carbon replacing titanium atom in the lattice of  $\text{TiO}_2$  to form a  $\text{Ti}-\text{O}-\text{C}$  structure (interstitial C-doping).<sup>67,68</sup> Thus, all C is adsorbed onto the surface but do not entered into the lattice of  $\text{TiO}_2$ .

Fig. 5c shows a high-resolution N 1s spectrum. After deconvolution, a single broad peak was observed at 400.21 eV

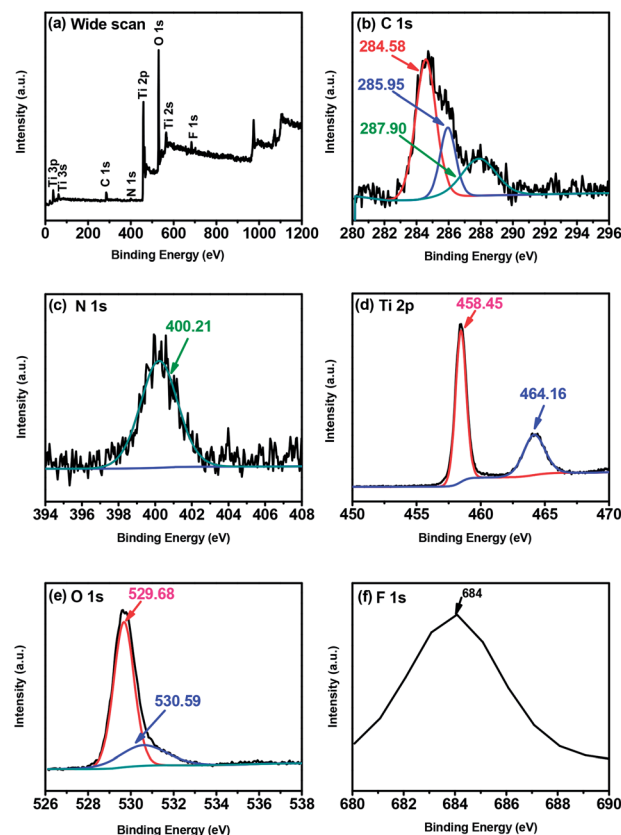


Fig. 5 XPS spectra of  $\text{TiO}_2$  nanocuboids prepared at 200 °C for 48 h (a) the wide scan (b) C 1s, (c) N 1s, (d) Ti 2p, (e) O 1s and (f) F 1s.

which can be assigned to pyrrolic nitrogen.<sup>69,70</sup> In general N 1s peak around 400 eV is typically assigned to the interstitial nitrogen dopant while the peak around 396 eV is associated to the substitutional nitrogen dopant. The N 1s peak at 400.21 eV arises due to the nitrogen species bonded to oxygen sites ( $\text{N}-\text{O}-\text{Ti}$  linkage); *i.e.* an interstitial N-doping mode formed by N-atoms bonded to one or more lattice oxygen atoms. The absence of peak around 396–397 eV due to Ti–N bonding ( $\text{O}-\text{Ti}-\text{N}$  linkage) exclude the possibility of substitutional N-doping for oxygen atoms in the  $\text{TiO}_2$  lattice.<sup>71,72</sup> These results indicate that N is only interstitially incorporated into the lattice of  $\text{TiO}_2$ . The origin of this N doping was either from the used  $\text{NH}_3$  or EDTA during the synthesis of  $\text{TiO}_2$  nanocuboids.

Fig. 5d shows the XPS spectrum of Ti 2p doublet peaks. The binding energies of Ti  $2p_{3/2}$  and Ti  $2p_{1/2}$  are located at approximately 458.45 eV and 464.16 eV, respectively. The splitting between the Ti  $2p_{1/2}$  and Ti  $2p_{3/2}$  core levels is 5.71 eV, indicating a normal state of  $\text{Ti}^{4+}$  in the  $\text{TiO}_2$ .<sup>66,73</sup>

As shown in Fig. 5e, the high-resolution O 1s spectrum is composed of two peaks. The major peak located at 529.68 eV is ascribed to lattice oxygen ( $\text{Ti}-\text{O}-\text{Ti}$ ),<sup>74,75</sup> whereas the small peak centered at 530.59 eV is due to the contributions from  $\text{C}=\text{O}$  or  $\text{O}=\text{C}-\text{OH}$ .<sup>76</sup>

Fig. 5f shows the high-resolution XPS spectrum of the F 1s region. A single peak observed around 684 eV is due to the surface fluoride ( $\equiv\text{Ti}-\text{F}$ ) formed by ligand exchange reaction





between  $F^-$  and the surface hydroxyl group on the surface of  $TiO_2$ .<sup>77,78</sup>  $TiO_2$  sample exhibited this peak, despite being washed the titanic acid precipitate several times with distilled water (and additionally with ethanol), indicating that the  $F^-$  ions (from HF) are bound to the surface. The peak around 688.5 eV is not observed indicating the absence of  $F^-$  ions in the lattice of  $TiO_2$ .<sup>77,79</sup> This indicates that F is only adsorbed on the surface of  $TiO_2$ .

The overall XPS results indicate that the C and F are adsorbed on the surface of  $TiO_2$  whereas N is doped at the interstitial sites of  $TiO_2$  lattice.

The shift of the (101) XRD peak toward lower  $2\theta$  value may be due to the presence of Ti–O–N–O linkages formed by interstitial doping of nitrogen in the lattice of  $TiO_2$ . The presence of oxidized nitrogen is due to the nitrogen substitution for titanium in  $TiO_2$  lattice.<sup>80</sup> Hsu *et al.* reported that N chemical states of the positively charged nitrogen species ( $N^{2+}$  or  $N^{3+}$ ) correspond to Ti–O–N–O linkage. Interstitial doping affects the lattice structure of N-doped  $TiO_2$ .<sup>81</sup>

### 3.4. FTIR analysis

Fourier transform infrared (FTIR) spectra of commercial  $TiO_2$  and  $TiO_2$  NCs prepared at 200 °C for 48 h are shown in Fig. S1 (ESI†). The bands located from 400–1000  $cm^{-1}$  are attributed to Ti–O stretching and Ti–O–Ti bridging stretching modes. A broad band observed in between 3000–3600  $cm^{-1}$  is due to the O–H stretching mode of hydroxyl group. The band at 1659  $cm^{-1}$  for  $TiO_2$  NCs prepared at 200 °C for 48 h can be attributed to the O=C–O–Ti bond of the carbonate structure, further confirming that doped carbon substituted surface Ti atoms to form a carbonate structure, while the band at 1645  $cm^{-1}$  for commercial  $TiO_2$  is due to the O–H bending vibrations of the adsorbed water molecules.<sup>82,83</sup>

The band at 1535  $cm^{-1}$  is assigned to the N–H in-plane bending vibration and C–N stretching vibration and the band at 1179  $cm^{-1}$  is due to C–N stretching.<sup>84</sup> No such nitrogen related bands are observed for commercial  $TiO_2$ , suggesting that the N species have been incorporated into the lattice of  $TiO_2$  nanocuboids.

### 3.5. UV-visible-DRS spectra

The UV-vis diffuse reflectance spectra of commercial  $TiO_2$  and as prepared  $TiO_2$  NCs are shown in Fig. 6a. The commercial  $TiO_2$  shows the typical optical absorption in the UV part of the spectrum whereas all of the as prepared  $TiO_2$  NCs show higher UV absorption intensity with a distinct new absorption tail in the visible light region (400–750 nm). Park *et al.*<sup>79</sup> have been reported that surface fluoride species are responsible for higher UV absorption whereas the absorption edge region is unaffected by the surface fluorination when F- $TiO_2$  is prepared around pH 3–4. However the enhanced absorption in the visible region (the tail) could be attributed to the interstitial N-doping as reported in the previous article<sup>61</sup> as well as the presence of carbonaceous and carbonate species on the surface of  $TiO_2$  NCs. The carbonaceous and carbonate species can act as a photosensitizer and could cause a long-tailed absorption in the visible-light region.<sup>65,85–87</sup> Thus  $TiO_2$  NCs can absorb more number of photons and can increase the number of photogenerated

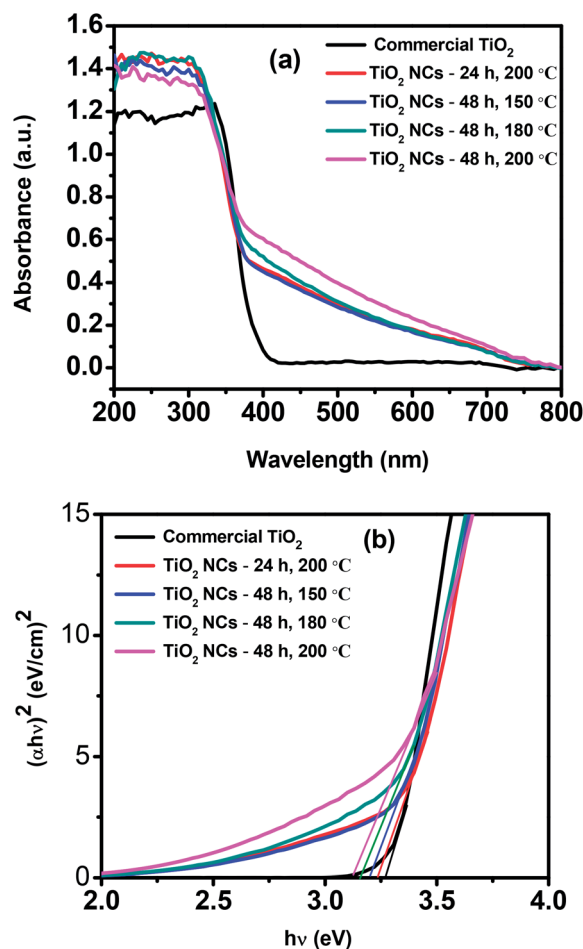


Fig. 6 (a) UV-visible diffuse reflectance spectra and (b) Tauc plots of commercial  $TiO_2$  and as prepared  $TiO_2$  nanocuboids.

electrons and holes to participate in the photocatalytic reaction. All these would enhance the photocatalytic activity of  $TiO_2$  NCs.

Band gap energies ( $E_g$ ) of the commercial  $TiO_2$  and as prepared  $TiO_2$  NCs can be estimated by using Tauc plots. Fig. 6b shows the plot of  $(\alpha h\nu)^2$  versus  $h\nu$ , where  $\alpha$  is the absorption coefficient and  $h\nu$  is the photon energy. The intercept of the tangent to the X axis gives the bandgap value. The band gap of commercial  $TiO_2$  was found to be 3.27 eV and for  $TiO_2$  NCs prepared at different reaction conditions, *i.e.* 24 h, 200 °C; 48 h, 150 °C; 48 h, 180 °C and 48 h, 200 °C, the band gap values were 3.24, 3.20, 3.16 and 3.12 eV respectively (Table 1).

It has been reported that, surface carbonaceous and carbonate species as well as interstitial nitrogen species (Ti–O–N) may not cause significant change of  $TiO_2$  band gap.<sup>60,65,88</sup> In the present report also, as compared to the band gap of commercial  $TiO_2$ , there was no considerable decrease of the band gap for as prepared  $TiO_2$  NCs and the band gap values are slightly lower than commercial  $TiO_2$ .

### 3.6. BET surface areas

The Brunauer–Emmett–Teller specific surface areas ( $S_{BET}$ ) of the commercial  $TiO_2$  and  $TiO_2$  NCs are listed in Table 1. The



specific surface area of commercial  $\text{TiO}_2$  powder was measured about  $29.3 \text{ m}^2 \text{ g}^{-1}$ . The measured surface areas of the  $\text{TiO}_2$  NCs prepared at different reaction conditions *i.e.* 24 h,  $200^\circ\text{C}$ ; 48 h,  $150^\circ\text{C}$ ; 48 h,  $180^\circ\text{C}$  and 48 h,  $200^\circ\text{C}$  were 122.9, 111.6, 103.2 and  $85.7 \text{ m}^2 \text{ g}^{-1}$  respectively. As can be seen from Table 1, the BET surface areas of the as prepared  $\text{TiO}_2$  NCs decrease with the increase of reaction time and temperature.

Fig. S2† shows the nitrogen adsorption-desorption isotherms and their corresponding pore size distributions of commercial  $\text{TiO}_2$  and as prepared  $\text{TiO}_2$  NCs. As shown in the Fig. S2a (ESI†), all of the samples exhibited isotherm of type IV (Brunauer–Deming–Deming–Teller (BDDT) classification) at relative pressure range of 0.7–1.0, associated with capillary condensation of gases within mesopores (2–50 nm). The isotherms show high adsorption at high relative pressure approaching 1.0, indicating the formation of large mesopores. Commercial  $\text{TiO}_2$  has lowest  $\text{N}_2$  volume adsorption indicating lower surface area as compared to other prepared  $\text{TiO}_2$  NCs. With increasing hydrothermal time and temperature, the hysteresis loops gradually became smaller with decrease in surface area of  $\text{TiO}_2$  NCs. The hysteresis loop is of type H3, which is consistent with slit shaped pores resulted from aggregates of plate-like particles.<sup>89</sup> Since the  $\text{TiO}_2$  nanocrystals themselves do not have any mesopores, these mesopores could be attributed to the aggregation of nanocrystals. These kind of organized porous structures might be useful in photocatalysis as they possess efficient transport pathways to reactant and product molecules. The corresponding pore size distribution of the samples is shown in Fig. S2b (ESI†). The pore size distribution of the samples is calculated from desorption branch of the nitrogen isotherm using the BJH (Barrett–Joyner–Halenda) method. Specific surface area, pore volume and average pore size of commercial  $\text{TiO}_2$  and as prepared  $\text{TiO}_2$  NCs are listed in Table S1 (ESI†). With rise in reaction time and temperature, the decrease of specific surface area is observed for  $\text{TiO}_2$  NCs. This may be due to the growth and coarsening of  $\text{TiO}_2$  NCs during the synthesis process.

### 3.7. Formation mechanism of the $\text{TiO}_2$ nanocuboids

The possible mechanism for the formation of  $\text{TiO}_2$  NCs is illustrated in Fig. 7. Commercial titanium(IV) oxide first react with hydrogen fluoride to produce dihydrogen hexafluorotitanate (hydrofluorotitanic acid,  $\text{H}_2\text{TiF}_6$ )<sup>90</sup> and water which is then neutralized with aqueous ammonia to give hydrated titanium oxide *i.e.* titanic acid ( $\text{H}_2\text{TiO}_3$ ) as shown in eqn (S1) and (S2) (ESI†). When  $\text{TiO}_2(\text{H}_2\text{O})$  *i.e.*  $\text{H}_2\text{TiO}_3$  (titanic acid) reacts with hydrogen peroxide and ammonia, ammonium peroxotitanate complex is formed<sup>91</sup> (eqn (S3)) (ESI†). This complex on further treatment with ethylenediamine tetraacetic acid (EDTA), forms ammonium peroxotitanate EDTA complex (eqn (S4)) (ESI†). Under hydrothermal condition this complex slowly decomposes and releases  $\text{O}_2$  to form  $\text{TiO}_2$  (eqn (S5)) (ESI†).

Initially, tiny nuclei of  $\text{TiO}_2$  are produced in the supersaturated solution and further growth of nanoparticles take place with time. The newly formed  $\text{TiO}_2$  nanoparticles are

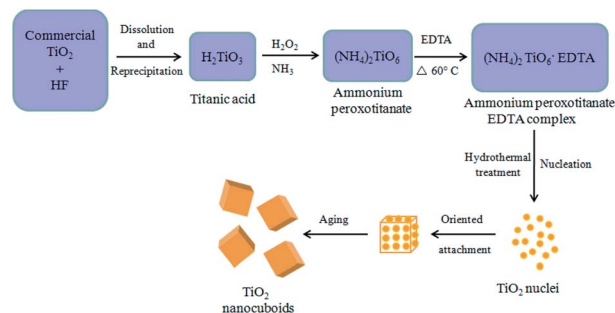


Fig. 7 A proposed mechanism for the formation of  $\text{TiO}_2$  nanocuboids.

spontaneously aggregated to minimize their surface energy. Here EDTA, prevents the agglomeration of  $\text{TiO}_2$  nanoparticles and controls their shape and morphology resulting in smaller sized particles. These nanoparticles further grow anisotropically along the 3D direction resulting in the formation of cuboid-like morphology.

### 3.8. Photocatalytic hydrogen generation

The photocatalytic performance of the commercial  $\text{TiO}_2$  and as prepared  $\text{TiO}_2$  NCs was evaluated with the photocatalytic hydrogen generation from water under UV-visible light irradiation. As shown in Fig. 8, the commercial  $\text{TiO}_2$  sample exhibited lowest  $\text{H}_2$  evolution activity that  $3325.22 \mu\text{mol}$  of  $\text{H}_2$  was generated in 4 h. However,  $\text{TiO}_2$  NCs prepared under different reaction time and temperature conditions showed enhanced photocatalytic  $\text{H}_2$  generation activity.

The cumulative amounts of  $\text{H}_2$  evolved in 4 h were 6825.62, 7697.26, 11 819.12 and  $15\ 465.78 \mu\text{mol}$  for the  $\text{TiO}_2$  NCs prepared for 24 h at  $200^\circ\text{C}$ , 48 h at  $150^\circ\text{C}$ , 48 h at  $180^\circ\text{C}$  and 48 h at  $200^\circ\text{C}$  respectively. Hydrogen generation rates of commercial and as prepared  $\text{TiO}_2$  NCs are summarized in Table 1. The higher photocatalytic activity of as prepared  $\text{TiO}_2$  NCs is due to the high specific surface areas in the range of  $85.7$ – $122.9 \text{ m}^2 \text{ g}^{-1}$ , much higher than that of commercial anatase  $\text{TiO}_2$  ( $29.3 \text{ m}^2 \text{ g}^{-1}$ ).

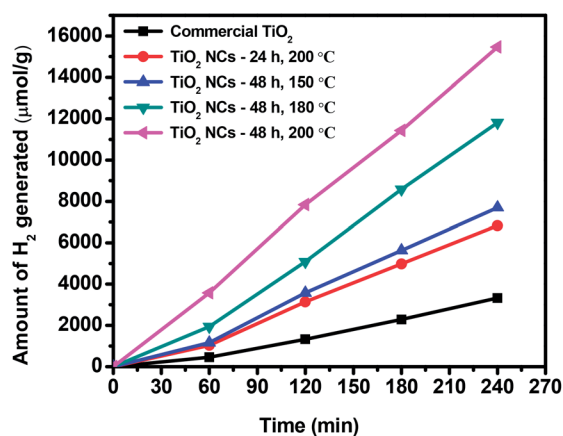


Fig. 8 Cumulative amount of hydrogen generated from the commercial  $\text{TiO}_2$  and  $\text{TiO}_2$  nanocuboids in 4 h of irradiation.



It is known that the photocatalytic performance of the photocatalyst depends on the two key factors, specific surface area and crystallinity. Photocatalysts with a high specific surface area offers a higher number of active sites and can provide short diffusion distances for electrons and holes to get to the surface active sites, thus limiting the recombination probability.<sup>92</sup> From Table 1 it can be observed that, among all of the as prepared TiO<sub>2</sub> NCs, NCs prepared at 200 °C for 48 h displays the smallest specific surface area *i.e.* 85.7 m<sup>2</sup> g<sup>-1</sup> but demonstrates the best photocatalytic activity than the TiO<sub>2</sub> NCs prepared at same temperature for 24 h and having higher specific surface area, *i.e.* 122.9 m<sup>2</sup> g<sup>-1</sup>. This is due to the slightly high relative crystallinity of the TiO<sub>2</sub> NCs prepared at 200 °C for 48 h. If the crystallinity is high, the charge carriers can reach the surface without getting trapped by the defects (that act as recombination centers of photogenerated carriers) which is helpful for enhancement of photocatalytic activity. The photoluminescence (PL) study can provide useful information about the efficiency of electron-hole recombination. The PL emission spectra of the prepared TiO<sub>2</sub> NCs with an excitation wavelength of 275 nm are presented in ESI† as Fig. S3.† The single PL emission peaks centered around 364 nm indicate the formation of defect free TiO<sub>2</sub> nanostructures. It is well reported that, higher emission peak intensity signifies higher recombination of photogenerated charge carriers which results in lowering of photocatalytic activity.<sup>53,73</sup> In our case, the same trend is observed *i.e.* TiO<sub>2</sub> NCs prepared at 200 °C for 24 h showed higher emission peak intensity and lower photocatalytic activity, whereas the TiO<sub>2</sub> NCs prepared at 200 °C for 48 h showed lower emission peak intensity and higher photocatalytic activity. Additionally, the good crystallinity observed in TiO<sub>2</sub> NCs prepared at 200 °C for 48 h is also responsible for higher photocatalytic activity because the crystallinity plays an important role than specific surface area in enhancing the photocatalytic activity.

In addition to the large surface area and high crystallinity, good light absorption capacity of photocatalysts and efficient charge separation of photogenerated electrons and holes also contribute to the high photocatalytic activity. All of the as prepared TiO<sub>2</sub> NCs exhibited higher photocatalytic H<sub>2</sub> generation efficiency in contrast to the commercial TiO<sub>2</sub> because of the improved light response in the range of 400–750 nm. We have used platinum (Pt) as a co-catalyst and methanol as a sacrificial reagent during the photocatalytic experiments to suppress the electron-hole recombination. Moreover, it has also been reported that surface fluorination can also greatly reduce the recombination of photogenerated electron-hole pairs, as surface ≡Ti-F groups can act as electron-trapping sites retaining photogenerated electrons due to the strong electronegativity of the fluoride. Thus, more efficient charge separation will be produced, leading therefore to the enhancement of the photocatalytic activity.<sup>11,75,76</sup>

Fig. 9 illustrates the mechanism of photocatalytic H<sub>2</sub> generation from water. When TiO<sub>2</sub> nanocuboid absorbs a photon with energy equal to or greater than its band gap, electrons are excited from the valence band (VB) to the conduction band (CB) leaving the holes in the VB. The photo-excited electrons and holes can migrate to the surface of the

TiO<sub>2</sub>. Electron-hole pairs that reach the surface without recombination, participate in the photocatalytic reactions of water splitting. Use of Pt as a co-catalyst and methanol as a sacrificial reagent helps to reduce the recombination of electrons and holes. As the bottom edge of the conduction band (CB) of TiO<sub>2</sub> is more negative than the H<sub>2</sub> evolution level (EH<sub>2</sub>/H<sub>2</sub>O), and the top edge of the valence band (VB) is more positive than the oxygen generation level (EH<sub>2</sub>O/O<sub>2</sub>), photoinduced electrons and holes react with the water adsorbed on the surface of TiO<sub>2</sub>. As a result, H<sup>+</sup> is reduced into H<sub>2</sub> and H<sub>2</sub>O is oxidized into O<sub>2</sub>.<sup>93,94</sup>

As discussed earlier and as shown in Table 1, the hydrogen evolution rate of the TiO<sub>2</sub> NCs prepared at 200 °C for 48 h (3866.44 μmol h<sup>-1</sup> g<sup>-1</sup>) is much higher than that of commercial TiO<sub>2</sub> (831.30 μmol h<sup>-1</sup> g<sup>-1</sup>). This 4.65-fold increase in the photocatalytic activity of TiO<sub>2</sub> NCs can be ascribed to the synergistic effect of high specific surface area, good crystallinity, enhanced light absorption in the range of 400–750 nm and effective separation of electron-hole pairs. This reported H<sub>2</sub> generation rate is also high as compared to the previous reports. Table S2 (ESI†) provides comparison of the H<sub>2</sub> generation activity of previously reported different anatase TiO<sub>2</sub> nanostructures with the anatase TiO<sub>2</sub> NCs presented in this work.

In order to evaluate the stability and the reusability of the catalyst, a recycling study of the most active sample *i.e.* TiO<sub>2</sub> NCs prepared at 200 °C for 48 h was carried out in terms of its photocatalytic hydrogen production. The same catalyst was recycled three times in the hydrogen generation reactions (Fig. 10). It is observed that the catalytic activity of TiO<sub>2</sub> NCs did not exhibit any significant loss in the second and third cycles. After third cycle, the amount of H<sub>2</sub> generated is around 14 770 μmol of H<sub>2</sub>, per g of recycled catalyst (*i.e.* 3692.50 μmol h<sup>-1</sup> g<sup>-1</sup>), indicating the high stability of the catalyst towards hydrogen generation.

To support higher photocatalytic activity of TiO<sub>2</sub> NCs prepared at 200 °C for 48 h, the photoconductivity measurements of all prepared TiO<sub>2</sub> NCs were carried out and compared with commercial TiO<sub>2</sub>.

### 3.9. Photoconductivity measurements

Photoconductivity measurements were carried out as per our previous report.<sup>95</sup> Fig. S4 (ESI†) shows *I-V* characteristics for

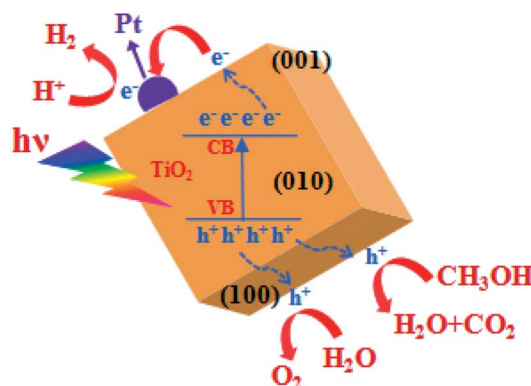


Fig. 9 Schematic illustration of the mechanism of photocatalytic H<sub>2</sub> generation from water over TiO<sub>2</sub> nanocuboid.





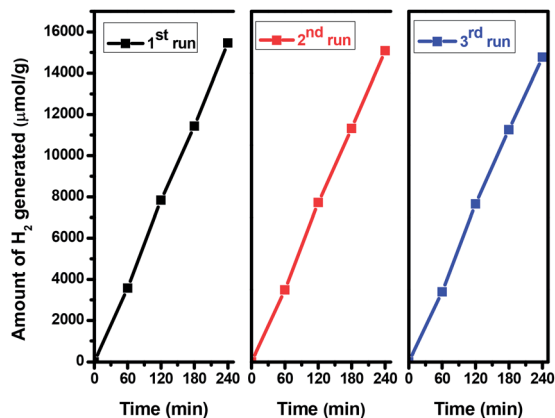


Fig. 10 Recyclability of the hydrogen generation behavior of  $\text{TiO}_2$  nanocuboids prepared at  $200^\circ\text{C}$  for 48 h.

commercial  $\text{TiO}_2$  and as prepared  $\text{TiO}_2$  NCs using two probes with applied bias voltage from  $-5\text{ V}$  to  $+5\text{ V}$  under illumination of light.  $I$ - $V$  measurements were carried out under  $1000\text{ W}$  xenon lamp and  $1.5$  (air-mass ratio). As can be seen from the inset of the figure, commercial  $\text{TiO}_2$  shows less response to photocurrent as compared to prepared  $\text{TiO}_2$  NCs. However photocurrent response increases as increase in the time and temperature conditions of  $\text{TiO}_2$  NCs. The highest photocurrent was observed for  $\text{TiO}_2$  NCs prepared at  $200^\circ\text{C}$  for 48 h. The two order enhanced photocurrent clearly correlate the enhanced photocatalytic performance of  $\text{TiO}_2$  NCs prepared at  $200^\circ\text{C}$  for 48 h as compared to other  $\text{TiO}_2$  NCs. This may be due to better crystallinity attributing higher photocatalytic performance as compared to other  $\text{TiO}_2$  NCs. In nutshell, the enhanced hydrogen evolution is due to nanostructuring of material along with good crystallinity.

## 4. Conclusions

Commercial anatase  $\text{TiO}_2$  was successfully modified into highly crystalline 3D NCs *via* hydrothermal method at different reaction time and temperature conditions.  $\text{TiO}_2$  NCs prepared at different time and temperature conditions found to have high specific surface area as compared to the commercial  $\text{TiO}_2$ . As prepared  $\text{TiO}_2$  NCs were explored for hydrogen production from photocatalytic water splitting. Obvious enhancement in the photocatalytic performance of the  $\text{TiO}_2$  NCs was demonstrated in  $\text{H}_2$  production, compared to the commercial  $\text{TiO}_2$ .  $\text{TiO}_2$  NCs obtained at  $200^\circ\text{C}$  for 48 h exhibited the highest photocatalytic  $\text{H}_2$  generation rate ( $3866.44\text{ }\mu\text{mol h}^{-1}\text{ g}^{-1}$ ), which is 4.65 times higher than that of commercial  $\text{TiO}_2$ . Also,  $\text{TiO}_2$  NCs exhibited the good cycling stability. The enhanced photocatalytic activity of  $\text{TiO}_2$  NCs obtained at  $200^\circ\text{C}$  for 48 h as compared to commercial  $\text{TiO}_2$  could be attributed to its large specific surface area, good crystallinity, extended visible light absorption and efficient separation of photo-induced carriers. The photoconductive study supports the higher photocatalytic performance of  $\text{TiO}_2$  NCs prepared at  $200^\circ\text{C}$  for 48 h. This study provides a simple and economical way to prepare highly active and

promising anatase  $\text{TiO}_2$  photocatalyst for hydrogen generation from water.

## Conflicts of interest

There are no conflicts to declare.

## Acknowledgements

Authors are grateful to Director, C-MET, Pune for providing the necessary characterization facility and for useful discussion. The authors are grateful to Ministry of Electronics and Information Technology (MeitY), Govt. of India, New Delhi for financial support.

## Notes and references

- 1 M. Humayun, F. Raziq, A. Khan and W. Luo, Modification strategies of  $\text{TiO}_2$  for potential applications in photocatalysis: a critical review, *Green Chem. Lett. Rev.*, 2018, **11**, 86–102.
- 2 Z. Bian, T. Tachikawa, P. Zhang, M. Fujitsuka and T. Majima, Au/ $\text{TiO}_2$  Superstructure-Based Plasmonic Photocatalysts Exhibiting Efficient Charge Separation and Unprecedented Activity, *J. Am. Chem. Soc.*, 2014, **136**, 458–465.
- 3 H. Huang, C. Wang, J. Huang, X. Wang, Y. Du and P. Yang, Structure inherited synthesis of N-doped highly ordered mesoporous  $\text{Nb}_2\text{O}_5$  as robust catalysts for improved visible light photoactivity, *Nanoscale*, 2014, **6**, 7274–7280.
- 4 Y. Li, Y.-K. Peng, L. Hu, J. Zheng, D. Prabhakaran, S. Wu, T. J. Puchler, M. Li, K.-Y. Wong, R. A. Taylor and S. C. E. Tsang, Photocatalytic water splitting by N- $\text{TiO}_2$  on  $\text{MgO}(111)$  with exceptional quantum efficiencies at elevated temperatures, *Nat. Commun.*, 2019, **10**, 4421.
- 5 A. Kudo and Y. Miseki, Heterogeneous photocatalyst materials for water splitting, *Chem. Soc. Rev.*, 2009, **38**, 253–278.
- 6 X. B. Chen, S. H. Shen, L. J. Guo and S. S. Mao, Semiconductor-based Photocatalytic Hydrogen Generation, *Chem. Rev.*, 2010, **110**, 6503–6570.
- 7 A. Fujishima and K. Honda, Electrochemical Photolysis of Water at a Semiconductor Electrode, *Nature*, 1972, **238**, 37–38.
- 8 W. Y. Teoh, J. A. Scott and R. Amal, Progress in Heterogeneous Photocatalysis: From Classical Radical Chemistry to Engineering Nanomaterials and Solar Reactors, *J. Phys. Chem. Lett.*, 2012, **3**, 629–639.
- 9 A. O. Ibadon and P. Fitzpatrick, Heterogeneous Photocatalysis: Recent Advances and Applications, *Catalysts*, 2013, **3**, 189–218.
- 10 G. L. Chiarello, M. V. Dozzi and E. Selli,  $\text{TiO}_2$ -based materials for photocatalytic hydrogen production, *J. Energy Chem.*, 2017, **26**, 250–258.
- 11 S. Kansal, P. Kundu, S. Sood, R. Lamba, A. Umar and S. K. Mehta, Photocatalytic degradation of antibiotic levofloxacin using well-crystalline  $\text{TiO}_2$  nanoparticles, *New J. Chem.*, 2014, **38**, 3220–3226.



- 12 Y. Wang, C. Sun, X. Zhao, B. Cui, Z. Zeng, A. Wang, G. Liu and H. Cui, The Application of Nano-TiO<sub>2</sub> Photo Semiconductors in Agriculture, *Nanoscale Res. Lett.*, 2016, **11**, 529.
- 13 V. Kumaravel, S. Mathew, J. Bartlett and S. C. Pillai, Photocatalytic hydrogen production using metal doped TiO<sub>2</sub>: A review of recent advances, *Appl. Catal., B*, 2019, **244**, 1021–1064.
- 14 S. Ge, D. Li, G. Jia, B. Wang, Z. Yang, Z. Yang, H. Qiao, Y. Zhang and Z. Zheng, Hydrofluoric Acid Controlled TiO<sub>2</sub> Phase Transformation from Rutile to Anatase at Room Temperature and Their Photocatalytic Performance, *J. Nanosci. Nanotechnol.*, 2015, **15**, 6636–6641.
- 15 L. Zhang, L. Tian, Y. Liu, T. Tan, D. Liu and C. Wang, Synthesis of tapered tetragonal nanorods of anatase TiO<sub>2</sub> with enhanced photocatalytic activity *via* a sol-hydrothermal process mediated by H<sub>2</sub>O<sub>2</sub> and NH<sub>3</sub>, *J. Mater. Chem. A*, 2015, **3**, 15265–15273.
- 16 L. Chen, Q. Gu, L. Hou, C. Zhang, Y. Lu, X. Wang and J. Long, Molecular p–n heterojunction-enhanced visible-light hydrogen evolution over N-doped TiO<sub>2</sub> photocatalyst, *Catal. Sci. Technol.*, 2017, **7**, 2039–2049.
- 17 M. Ismael, Highly effective ruthenium-doped TiO<sub>2</sub> nanoparticles photocatalyst for visible-light-driven photocatalytic hydrogen production, *New J. Chem.*, 2019, **43**, 9596–9605.
- 18 N. Vinothkumar and M. De, Enhanced photocatalytic hydrogen production from water methanol mixture using cerium and nonmetals (B/C/N/S) co-doped titanium dioxide, *Mater. Renew. Sustain. Energy*, 2014, **3**, 25.
- 19 Y. Yang, D. Ni, Y. Yao, Y. Zhong, Y. Ma and J. Yao, High photocatalytic activity of carbon doped TiO<sub>2</sub> prepared by fast combustion of organic capping ligands, *RSC Adv.*, 2015, **5**, 93635–93643.
- 20 M. Murdoch, G. I. N. Waterhouse, M. A. Nadeem, J. B. Metson, M. A. Keane, R. F. Howe, J. Llorca and H. Idriss, The effect of gold loading and particle size on photocatalytic hydrogen production from ethanol over Au/TiO<sub>2</sub> nanoparticles, *Nat. Chem.*, 2011, **3**, 489–492.
- 21 J. M. Valero, S. Obregón and G. Colon, Active Site Considerations on the Photocatalytic H<sub>2</sub> Evolution Performance of Cu-Doped TiO<sub>2</sub> Obtained by Different Doping Methods, *ACS Catal.*, 2014, **4**, 3320–3329.
- 22 M.-C. Wu, A. Sapi, A. Avila, M. Szabo, J. Hiltunen, M. Huuhtanen, G. Toth, A. Kukovecz, Z. Konya, R. Keiski, W.-F. Su, H. Jantunen and K. Kordas, Enhanced Photocatalytic Activity of TiO<sub>2</sub> Nanofibers and Their Flexible Composite Films: Decomposition of Organic Dyes and Efficient H<sub>2</sub> Generation from Ethanol–Water Mixtures, *Nano Res.*, 2011, **4**, 360–369.
- 23 A. M. Hussein, L. Mahoney, R. Peng, H. Kibombo, C.-M. Wu, R. T. Koodali and R. Shende, Mesoporous coupled ZnO/TiO<sub>2</sub> photocatalyst nanocomposites for hydrogen generation, *J. Renewable Sustainable Energy*, 2013, **5**, 033118.
- 24 J. Fang, L. Xu, Z. Zhang, Y. Yuan, S.-W. Cao, Z. Wang, L. Yin, Y. Liao and C. Xue, Au@TiO<sub>2</sub>-CdS Ternary Nanostructures for Efficient Visible-light-Driven Hydrogen Generation, *ACS Appl. Mater. Interfaces*, 2013, **5**, 8088–8092.
- 25 Y. Lin, P. Ren and C. Wei, Fabrication of MoS<sub>2</sub>/TiO<sub>2</sub> heterostructure with enhanced photocatalytic activity, *CrystEngComm*, 2019, **21**, 3439–3450.
- 26 Y. Yamazaki, K. Azami, R. Katoh and S. Yamazaki, Developing Active TiO<sub>2</sub> Nanorods by Examining the Influence of Morphological Changes from Nanorods to Nanoparticles on Photocatalytic Activity, *ACS Appl. Nano Mater.*, 2018, **1**, 5927–5935.
- 27 M. Shahrezaei, S. Habibzadeh, A. A. Babaluo, H. Hosseinkhani, M. Haghighi, A. Hasanzadeh and R. Tahmasebpour, Study of synthesis parameters and photocatalytic activity of TiO<sub>2</sub> nanostructures, *J. Exp. Nanosci.*, 2017, **12**, 45–61.
- 28 Y. Du, W. Li, Y. Bai, Z. Huangfu, W. Wang, R. Chai, C. Chen, X. Yang and Q. Feng, Facile synthesis of TiO<sub>2</sub>/Ag<sub>3</sub>PO<sub>4</sub> composites with co-exposed high-energy facets for efficient photodegradation of rhodamine B solution under visible light irradiation, *RSC Adv.*, 2020, **10**, 24555–24569.
- 29 Y. Du, X. Niu, J. He, L. Liu, Y. Liu, C. Chen, X. Yang and Q. Feng, Hollow Square RodLike Microtubes Composed of Anatase Nanocuboids with Coexposed {100}, {010}, and {001} Facets for Improved Photocatalytic Performance, *ACS Omega*, 2020, **5**, 14147–14156.
- 30 O. Sacco, Di. Sannino, M. Matarangolo and V. Vaiano, Room Temperature Synthesis of V-Doped TiO<sub>2</sub> and Its Photocatalytic Activity in the Removal of Caffeine under UV Irradiation, *Materials*, 2019, **12**, 911.
- 31 D. He and F. Lin, Preparation and photocatalytic activity of anatase TiO<sub>2</sub> nanocrystallites with high thermal stability, *Mater. Lett.*, 2007, **61**, 3385–3387.
- 32 R. Acharya, B. Naik and K. Parida, Cr(VI) remediation from aqueous environment through modified-TiO<sub>2</sub>-mediated photocatalytic reduction, *Beilstein J. Nanotechnol.*, 2018, **9**, 1448–1470.
- 33 K. Zimny, T. Roques-Carnes, C. Carteret, M. J. Stebe and J. L. Blin, Synthesis and Photoactivity of Ordered Mesoporous Titania with a Semicrystalline Framework, *J. Phys. Chem. C*, 2012, **116**, 6585–6594.
- 34 Y.-F. Li and Z.-P. Liu, Particle Size, Shape and Activity for Photocatalysis on Titania Anatase Nanoparticles in Aqueous Surroundings, *J. Am. Chem. Soc.*, 2011, **133**, 15743–15752.
- 35 H. Yang, K. Zhang, R. Shi, X. Li, X. Dong and Y. Yu, Sol-gel synthesis of TiO<sub>2</sub> nanoparticles and photocatalytic degradation of methyl orange in aqueous TiO<sub>2</sub> suspensions, *J. Alloys Compd.*, 2006, **413**, 302–306.
- 36 S. Lee, I.-S. Cho, J. H. Lee, D. H. Kim, D. W. Kim, J. Y. Kim, H. Shin, J.-K. Lee, H. S. Jung, N.-G. Park, K. Kim, M. J. Ko and K. S. Hong, Two-Step Sol-Gel Method-Based TiO<sub>2</sub> Nanoparticles with Uniform Morphology and Size for Efficient Photo-Energy Conversion Devices, *Chem. Mater.*, 2010, **22**, 1958–1965.
- 37 J.-N. Nian and H. Teng, Hydrothermal Synthesis of Single-Crystalline Anatase TiO<sub>2</sub> Nanorods with Nanotubes as the Precursor, *J. Phys. Chem. B*, 2006, **110**, 4193–4198.
- 38 X. Niu, Y. Du, Y. Liu, H. Qi, J. An, X. Yang and Q. Feng, Hydrothermal synthesis and formation mechanism of the



- anatase nanocrystals with co-exposed high energy {001}, {010} and [111]-facets for enhanced photocatalytic performance, *RSC Adv.*, 2017, 7, 24616–24627.
- 39 A. Jena, R. Vinu, S. A. Shivashankar and G. Madras, Microwave Assisted Synthesis of Nanostructured Titanium Dioxide with High Photocatalytic Activity, *Ind. Eng. Chem. Res.*, 2010, 49, 9636–9643.
  - 40 Y. Chimupala, G. Hyett, R. Simpson, R. Mitchell, R. Douthwaite, S. J. Milne and R. D. Brydson, Synthesis and characterization of mixed phase anatase TiO<sub>2</sub> and sodium-doped TiO<sub>2</sub>(B) thin films by low pressure chemical vapour deposition (LPCVD), *RSC Adv.*, 2014, 4, 48507–48515.
  - 41 M. Dhiman, R. Sharma, V. Kumar and S. Singhal, Morphology controlled hydrothermal synthesis and photocatalytic properties of ZnFe<sub>2</sub>O<sub>4</sub> nanostructures, *Ceram. Int.*, 2016, 42, 12594–12605.
  - 42 H. Yin, G. Ding, B. Gao, F. Huang, X. Xie and M. Jiang, Synthesis of ultrafine titanium dioxide nanowires using hydrothermal method, *Mater. Res. Bull.*, 2012, 47, 3124–3128.
  - 43 K. C. Sun, M. B. Qadir and S. H. Jeong, Hydrothermal synthesis of TiO<sub>2</sub> nanotubes and their application as an over-layer for dye-sensitized solar cells, *RSC Adv.*, 2014, 4, 23223–23230.
  - 44 P. Hu, G. Du, W. Zhou, J. Cui, J. Lin, H. Liu, D. Liu, J. Wang and S. Chen, Enhancement of Ethanol Vapor Sensing of TiO<sub>2</sub> Nanobelts by Surface Engineering, *ACS Appl. Mater. Interfaces*, 2010, 2, 3263–3269.
  - 45 K. Santhi, M. Navaneethan, S. Harish, S. Ponnusamy and C. Muthamizhchelvan, Synthesis and characterization of TiO<sub>2</sub> nanorods by hydrothermal method with different pH conditions and their photocatalytic activity, *Appl. Surf. Sci.*, 2020, 500, 144058.
  - 46 W. Zhang, Y. Xie, D. Xiong, X. Zeng, Z. Li, M. Wang, Y.-B. Cheng, W. Chen, K. Yan and S. Yang, TiO<sub>2</sub> Nanorods: A Facile Size- and Shape-Tunable Synthesis and Effective Improvement of Charge Collection Kinetics for Dye-Sensitized Solar Cells, *ACS Appl. Mater. Interfaces*, 2014, 6, 9698–9704.
  - 47 X. Han, Q. Kuang, M. Jin, Z. Xie and L. Zheng, Synthesis of Titania Nanosheets with a High Percentage of Exposed (001) Facets and Related Photocatalytic Properties, *J. Am. Chem. Soc.*, 2009, 131, 3152–3153.
  - 48 C. Wang, L. Yin, L. Zhang, Y. Qi, N. Lun and N. Liu, Large Scale Synthesis and Gas-Sensing Properties of Anatase TiO<sub>2</sub> Three-Dimensional Hierarchical Nanostructures, *Langmuir*, 2010, 26, 12841–12848.
  - 49 T. Zhu, J. Li and Q. Wu, Construction of TiO<sub>2</sub> Hierarchical Nanostructures from Nanocrystals and Their Photocatalytic Properties, *ACS Appl. Mater. Interfaces*, 2011, 3, 3448–3453.
  - 50 Y. Yang, J. X. Hu, Y. Liang, J. P. Zou, K. Xu, R. J. Hu, Z. D. Zou, Q. Yuan, Q. Q. Chen, Y. Lu, T. Yu and C. L. Yuan, Anatase TiO<sub>2</sub> hierarchical microspheres consisting of truncated nanothorns and their structurally enhanced gas sensing performance, *J. Alloys Compd.*, 2017, 694, 292–299.
  - 51 J. Yu, L. Qi and M. Jaroniec, Hydrogen Production by Photocatalytic Water Splitting over Pt/TiO<sub>2</sub> Nanosheets with Exposed (001) Facets, *J. Phys. Chem. C*, 2010, 114, 13118–13125.
  - 52 J. Jitputti, T. Rattanaavoravipa, S. Chuangchote, S. Pavasupree, Y. Suzuki and S. Yoshikawa, Low temperature hydrothermal synthesis of monodispersed flower-like titanate nanosheets, *Catal. Commun.*, 2009, 10, 378–382.
  - 53 G. Cheng, Y. Wei, J. Xiong, Y. Gan, J. Zhu and F. Xu, Same titanium glycolate precursor but different products: Successful synthesis of twinned anatase TiO<sub>2</sub> nanocrystals with excellent solar photocatalytic hydrogen evolution capability, *Inorg. Chem. Front.*, 2017, 4, 1319–1329.
  - 54 S. Ida, P. Wilson, B. Neppolian, M. Sathish, P. Karthik and P. Ravi, Ultrasonically aided selective stabilization of pyrrolic type nitrogen by one pot nitrogen doped and hydrothermally reduced Graphene oxide/Titania nanocomposite (N-TiO<sub>2</sub>/N-RGO) for H<sub>2</sub> production, *Ultrason. Sonochem.*, 2019, 57, 62–72.
  - 55 B. Wu, C. Guo, N. Zheng, Z. Xie and G. D. Stucky, Nonaqueous Production of Nanostructured Anatase with High-Energy Facets, *J. Am. Chem. Soc.*, 2008, 130, 17563–17567.
  - 56 N. T. Padmanabhan, P. Ganguly, S. C. Pillai and H. John, Morphology engineered spatial charge separation in superhydrophilic TiO<sub>2</sub>/graphene hybrids for hydrogen production, *Mater. Today Energy*, 2020, 17, 100447.
  - 57 Q. Huang, S. Tian, D. Zeng, X. Wang, W. Song, Y. Li, W. Xiao and C. Xie, Enhanced photocatalytic activity of chemically bonded TiO<sub>2</sub>/graphene composites based on the effective interfacial charge transfer through C-Ti bond, *ACS Catal.*, 2013, 3, 1477–1485.
  - 58 T. Hu, X. Sun, H. Sun, G. Xin, D. Shao, C. Liu and J. Lian, Rapid Synthesis of Nitrogen-Doped Graphene for Lithium ion Battery Anode with Excellent Rate Performance and Super-long Cyclic Stability, *Phys. Chem. Chem. Phys.*, 2014, 16, 1060–1066.
  - 59 Y. Dong, H. Pang, H. B. Yang, C. Guo, J. Shao, Y. Chi, C. M. Li and T. Yu, Carbon-Based Dots Co-doped with Nitrogen and Sulfur for High Quantum Yield and Excitation-Independent Emission, *Angew. Chem., Int. Ed.*, 2013, 52, 7800–7804.
  - 60 G.-S. Shao, L. Liu, T.-Y. Ma, F.-Y. Wang, T.-Z. Ren and Z.-Y. Yuan, Synthesis and characterization of carbon-modified titania photocatalysts with a hierarchical meso-/macroporous structure, *Chem. Eng. J.*, 2010, 160, 370–377.
  - 61 A.-Y. Zhang, L.-L. Long, C. Liu, W.-W. Li and H.-Q. Yu, Chemical recycling of the waste anodic electrolyte from the TiO<sub>2</sub> nanotube preparation process to synthesize facet-controlled TiO<sub>2</sub> single crystals as an efficient photocatalyst, *Green Chem.*, 2014, 16, 2745–2753.
  - 62 W. Zhu, H. Song, L. Zhang, Y. Weng, Y. Su and Y. Lv, Fabrication of Fluorescent Nitrogen-Rich Graphene Quantum Dots by Tin (IV) Catalytic Carbonization of Ethanolamine, *RSC Adv.*, 2015, 5, 60085–60089.
  - 63 J. Guo, Y. Shi, H. Zhou, X. Wang and T. Ma, A novel composite of W<sub>18</sub>O<sub>49</sub> nanorods on reduced graphene oxide sheets based on *in situ* synthesis and catalytic performance for oxygen reduction reaction, *RSC Adv.*, 2017, 7, 2051–2057.





- 64 J. P. H. Li, X. Zhou, Y. Pang, L. Zhu, E. I. Vovk, L. Cong, A. P. Bavel, S. Li and Y. Yang, Understanding of binding energy calibration in XPS of lanthanum oxide by *in situ* treatment, *Phys. Chem. Chem. Phys.*, 2019, **21**, 22351–22358.
- 65 X. Wang, Y. Tang, M.-Y. Lei and T.-T. Lim, Solvothermal synthesis of Fe–C codoped TiO<sub>2</sub> nanoparticles for visible-light photocatalytic removal of emerging organic contaminants in water, *Appl. Catal., A*, 2011, **409–410**, 257–266.
- 66 N. G. Moustakas, A. G. Kontos, V. Likodimos, F. Katsaros, N. Boukos, D. Tsoutsou, A. Dimoulas, G. E. Romanos, D. D. Dionysiou and P. Falaras, Inorganic–organic core-shell titania nanoparticles for efficient visible light activated photocatalysis, *Appl. Catal., B*, 2013, **130–131**, 14–24.
- 67 S. K. Warkhade, G. S. Gaikwad, S. P. Zodape, U. Pratap, A. V. Maldhure and A. V. Wankhade, Low temperature synthesis of pure anatase carbon doped titanium dioxide: An efficient visible light active photocatalyst, *Mater. Sci. Semicond. Process.*, 2017, **63**, 18–24.
- 68 W. Ren, Z. Ai, F. Jia, L. Zhang, X. Fan and Z. Zou, Low temperature preparation and visible light photocatalytic activity of mesoporous carbon-doped crystalline TiO<sub>2</sub>, *Appl. Catal., B*, 2007, **69**, 138–144.
- 69 H. Wang, T. Maiyalagan and X. Wang, Review on Recent Progress in Nitrogen-Doped Graphene: Synthesis, Characterization, and Its Potential Applications, *ACS Catal.*, 2012, **2**, 781–794.
- 70 F. M. Hassan, V. Chabot, J. Li, B. K. Kim, L. Ricardez-Sandoval and A. Yu, Pyrrolic-structure enriched nitrogen doped graphene for highly efficient next generation supercapacitors, *J. Mater. Chem. A*, 2013, **1**, 2904–2912.
- 71 C. Bittencourt, M. Rutar, P. Umek, A. Mrzel, K. Vozel, D. Arcon, K. Henzler, P. Kruger and P. Guttmann, Molecular nitrogen in N-doped TiO<sub>2</sub> nanoribbons, *RSC Adv.*, 2015, **5**, 23350–23356.
- 72 C. Yan, K.-F. Chen, C.-H. Lai, S.-W. Lai, Q. Chang and Y.-P. Peng, Photocatalytic degradation of Rhodamine B by microwave-assisted hydrothermal synthesized N-doped titanate nanotubes, *J. Environ. Sci.*, 2014, **26**, 1505–1512.
- 73 S. S. Thind, C. C. Mustapic, J. Wen, C. D. Goodwin and A. Chen, Facile synthesis of mesoporous carbon nitride and titanium dioxide nanocomposites with enhanced visible light photocatalytic activity, *New J. Chem.*, 2017, **41**, 10542–10549.
- 74 P. Zhang, C. Shao, Z. Zhang, M. Zhang, J. Mu, Z. Guo and Y. Liu, TiO<sub>2</sub>@carbon core/shell nanofibers: Controllable preparation and enhanced visible photocatalytic properties, *Nanoscale*, 2011, **3**, 2943–2949.
- 75 J. C. Xu, J. J. Zhang, Z. Y. Cai, H. Huang, T. H. Huang, P. Wang and X. Y. Wang, Facile and Large-scale Synthesis of Defective Black TiO<sub>2-x</sub>(B) Nanosheets for Efficient Visible-light-driven Photocatalytic Hydrogen Evolution, *Catalysts*, 2019, **9**, 1048.
- 76 D. Yang, A. Velamakanni, G. Bozoklu, S. Park, M. Stoller, R. D. Piner, S. Stankovich, I. Jung, D. A. Field, C. A. Ventrice Jr and R. S. Ruoff, Chemical analysis of graphene oxide films after heat and chemical treatments by X-ray photoelectron and Micro-Raman spectroscopy, *Carbon*, 2009, **47**, 145–152.
- 77 J. Yu, W. Wang, B. Cheng and B.-L. Su, Enhancement of Photocatalytic Activity of Mesoporous TiO<sub>2</sub> Powders by Hydrothermal Surface Fluorination Treatment, *J. Phys. Chem. C*, 2009, **113**, 6743–6750.
- 78 J. J. Murcia, M. C. Hidalgo, J. A. Navio, J. Arana and J. M. Dona-Rodriguez, Study of the phenol photocatalytic degradation over TiO<sub>2</sub> modified by sulfation, fluorination, and platinum nanoparticles photodeposition, *Appl. Catal., B*, 2015, **179**, 305–312.
- 79 H. Park and W. Choi, Effects of TiO<sub>2</sub> Surface Fluorination on Photocatalytic Reactions and Photoelectrochemical Behaviors, *J. Phys. Chem. B*, 2004, **108**, 4086–4093.
- 80 F. Peng, L. Cai, L. Huang, H. Yu and H. Wang, Preparation of nitrogen-doped titanium dioxide with visible-light photocatalytic activity using a facile hydrothermal method, *J. Phys. Chem. Solids*, 2008, **69**, 1657–1664.
- 81 J.-C. Hsu, Y.-H. Lin and P. W. Wang, X-ray Photoelectron Spectroscopy Analysis of Nitrogen-Doped TiO<sub>2</sub> Films Prepared by Reactive-Ion-Beam Sputtering with Various NH<sub>3</sub>/O<sub>2</sub> Gas Mixture Ratios, *Coatings*, 2020, **10**, 47.
- 82 P. Praveen, G. Viruthagiri, S. Mugundan and N. Shanmugam, Structural, optical and morphological analyses of pristine titanium di-oxide nanoparticles – Synthesized *via* sol-gel route, *Spectrochim. Acta, Part A*, 2014, **117**, 622–629.
- 83 C. Zhang, A. Cao, L. Chen, K. Lv, T. Wu and K. Deng, One-step topological preparation of carbon doped and coated TiO<sub>2</sub> hollow nanocubes for synergistically enhanced visible photodegradation activity, *RSC Adv.*, 2018, **8**, 21431–21443.
- 84 W. Xu, X. Yin, G. He, J. Zhao and H. Wang, Photografted temperature-sensitive poly(N-isopropylacrylamide) thin film with a superfast response rate and an interesting transparent–opaque–transparent change in its deswelling process, *Soft Matter*, 2012, **8**, 3105–3111.
- 85 C. Lettmann, K. Hildenbrand, H. Kisch, W. Macyk and W. F. Maier, Visible light photodegradation of 4-chlorophenol with a coke-containing titanium dioxide photocatalyst, *Appl. Catal., B*, 2001, **32**, 215–227.
- 86 X. Yang, C. Cao, K. Hohn, L. Erickson, R. Maghirang, D. Hamal and K. Klabunde, Highly visible-light active C- and V-doped TiO<sub>2</sub> for degradation of acetaldehyde, *J. Catal.*, 2007, **252**, 296–302.
- 87 Y.-T. Lin, C.-H. Weng, Y.-H. Lin, C.-C. Shiesh and F.-Y. Chen, Effect of C content and calcination temperature on the photocatalytic activity of C-doped TiO<sub>2</sub> catalyst, *Sep. Purif. Technol.*, 2013, **116**, 114–123.
- 88 D. Nassoko, Y.-F. Li, H. Wang, J.-L. Li, Y.-Z. Li and Y. Yu, Nitrogen-doped TiO<sub>2</sub> nanoparticles by using EDTA as nitrogen source and soft template: Simple preparation, mesoporous structure, and photocatalytic activity under visible light, *J. Alloys Compd.*, 2012, **540**, 228–235.
- 89 B. Wang, L. Guo, M. He and T. He, Green synthesis of TiO<sub>2</sub> nanocrystals with improved photocatalytic activity by ionic-liquid assisted hydrothermal method, *Phys. Chem. Chem. Phys.*, 2013, **15**, 9891–9898.



- 90 D. L. Dolcater, J. K. Syers and M. L. Jackson, Titanium As Free Oxide And Substituted Forms In Kaolinites And Other Soil Minerals, *Clays Clay Miner.*, 1970, **18**, 71–79.
- 91 F. Wu, X. Li, Z. Wang, L. Wu, H. Guo, X. Xiong, X. Zhang and X. Wang, Hydrogen peroxide leaching of hydrolyzed titania residue prepared from mechanically activated Panzhihua ilmenite leached by hydrochloric acid, *Int. J. Miner. Process.*, 2011, **98**, 106–112.
- 92 T. Jafari, E. Moharreri, A. S. Amin, R. Miao, W. Song and S. L. Suib, Photocatalytic water splitting—the untamed dream: a review of recent advances, *Molecules*, 2016, **21**, 900.
- 93 C.-H. Liao, C.-W. Huang and J. C. S. Wu, Hydrogen production from semiconductor-based photocatalysis *via* water splitting, *Catalysts*, 2012, **2**, 490–516.
- 94 M. Ni, M. K. H. Leung, D. Y. C. Leung and K. Sumathy, A review and recent developments in photocatalytic water-splitting using TiO<sub>2</sub> for hydrogen production, *Renewable Sustainable Energy Rev.*, 2007, **11**, 401–425.
- 95 S. R. Damkale, S. S. Arbuj, G. G. Umarji, R. P. Panmand, S. K. Khore, R. S. Sonawane, S. B. Rane and B. B. Kale, Two dimensional hexagonal SnS<sub>2</sub> nanostructures for photocatalytic hydrogen generation and dye degradation, *Sustainable Energy Fuels*, 2019, **3**, 3406–3414.

